applied optics

Label-free color staining of quantitative phase images of biological cells by simulated Rheinberg illumination

Xin Fan,[1] John J. Healy,[2] Kevin O'Dwyer,[1] and Bryan M. Hennelly[1,3,*]

[1]National University of Ireland, Department of Electronic Engineering, Maynooth, County Kildare, Ireland
[2]University College Dublin, School of Electrical and Electronic Engineering, Ireland
[3]National University of Ireland, Department of Computer Science, Maynooth, County Kildare, Ireland
*Corresponding author: bryanh@cs.nuim.ie

Received 21 November 2018; revised 12 March 2019; accepted 18 March 2019; posted 18 March 2019 (Doc. ID 352599); published 15 April 2019

Modern microscopes are designed with functionalities that are tailored to enhance image contrast. Dark-field imaging, phase contrast, differential interference contrast, and other optical techniques enable biological cells and other phase-only objects to be visualized. Quantitative phase imaging refers to an emerging set of techniques that allow for the complex transmission function of the sample to be measured. With this quantitative phase image available, any optical technique can then be simulated; it is trivial to generate a phase contrast image or a differential interference contrast image. Rheinberg illumination, proposed almost a century ago, is an optical technique that applies color contrast to images of phase-only objects by introducing a type of optical staining via an amplitude filter placed in the illumination path that consists of two or more colors. In this paper, the complete theory of Rheinberg illumination is derived, from which an algorithm is proposed that can digitally simulate the technique. Results are shown for a number of quantitative phase images of diatom cells obtained via digital holographic microscopy. The results clearly demonstrate the potential of the technique for label-free color staining of subcellular features.

https://doi.org/10.1364/AO.58.003104

1. INTRODUCTION

Unstained objects, such as biological cells, present a unique problem for the light microscopist because their images generate very little contrast and are essentially invisible in ordinary bright-field microscopy [1,2]. Transparent "phase-only" objects, such as biological cells, induce a spatially varying phase delay on the illuminating optical wavefield; this phase delay results from spatial variation in the specimen's refractive index and/or thickness. Phase-only objects remain nearly invisible in the image plane of the microscope, because physical detectors such as the eye, or a camera, cannot detect variation in phase. The diffraction pattern resulting from the phase delay introduced by the sample can be observed in other defocused planes, but such an approach renders the image difficult to interpret [1]. Several specialized imaging techniques [1–14] are commonly employed in light microscopes in order to enhance image contrast and enable a direct visualization of subcellular features (as well as other types of samples that induce small phase delays) without staining, such as dark field [1,2], phase contrast [3–5], differential interference contrast [6–8] (DIC), fluorescence [9,10], and Rheinberg illumination [11–14]. By exploiting refraction, diffraction, interference, or fluorescence, these methods are applied mainly to make visible objects such as cells and other biological structures that are otherwise invisible. Compared to bright-field microscopy, the optical images produced with such contrast techniques usually provide an unnatural appearance to the observed specimens. However, these approaches have become an essential set of tools for modern life science and material science research.

Although not as popular as phase contrast or DIC, Rheinberg illumination [11–14] is one such technique that provides a form of optical staining. The approach was initially demonstrated by the British microscopist Julius Rheinberg to the Royal Microscopical Society and the Quekett Club (England) in 1861. In Rheinberg illumination, diffraction effects are combined with selective absorption of light in certain parts of the specimen, in order to generate color contrast of subcellular features. In simple terms, for the case of a Rheinberg filter composed of a green center surrounded by a red ring, the image can be described as being similar to a dark-field image making up the red component of the image, superimposed on a lower-frequency green image that will include the background.

In this paper the underlying theory of Rheinberg illumination is investigated in detail and based on this, an algorithm is proposed that color stains cell images that have been recorded using quantitative phase microscopy.

Techniques such as phase contrast [3–5] and DIC [6–8] effectively enhance the contrast in images of phase-only objects. However, the information obtained with these techniques is essentially qualitative. Quantitative phase imaging (QPI) [15,16] provides a powerful means to study cellular dynamics associated with both thickness and refractive index fluctuations. QPI refers to a set of techniques that are capable of recording an accurate quantitative measurement of the phase delay imparted by the sample, and therefore provide the complex transmittance of the sample. This set of techniques includes digital holographic microscopy (DHM) [17–19], which makes use of a temporally coherent source to record an interference pattern between the image of the sample and a known reference wave field. In this paper, DHM is employed to record the complex transmittance of a number of diatom cells, which are used for testing the proposed color staining algorithm. Key advantages of DHM are a large depth of field [18,19], the capacity for computational aberration compensation to improve image quality [20,21], as well as the capability to refocus the image using numerical propagation algorithms [22,23], which can be used with autofocus metrics for automatic focusing over a wide depth of field [24,25]. In recent years QPI has been shown to be possible with white light [15,16,26–31], which produces significantly less noise due to the lower spatiotemporal coherence, and also using a form of lensless microscopy [32–34]. It can be expected that such methods will be commonplace in life science microscopy in the near future. A brief review of these methods is provided in Section 5.

The breakdown of this paper is as follows. In Section 2 the theory of optical Rheinberg illumination is derived. From this a numerical algorithm is proposed in Section 3 that can color stain subcellular features in complex transmittance images recorded using QPI techniques. In Section 4 the results are shown of applying the algorithm to a number of images of diatom cells recorded using DHM, and finally, in Section 5 a brief discussion is offered.

2. THEORY OF OPTICAL RHEINBERG ILLUMINATION

In this section, a theoretical framework for understanding optical staining by Rheinberg illumination is proposed. Despite the longevity of Rheinberg illumination, a search of the literature did not provide any theoretical analysis of the detail provided here. We believe that this work may represent the first detailed theoretical analysis of this type of imaging. In the next section, an algorithm is developed that is based on this analysis. In Fig. 1(a) the optical setup for Rheinberg illumination is illustrated. This setup is based on the traditional architecture of a bright-field optical microscope employing Kohler illumination [1,35]. In this configuration, a multimodal filter containing at least two color filters (most commonly in the form of a circle of one color filter around which is a ring containing a second color filter) is placed in the focal plane of the condenser lens. The

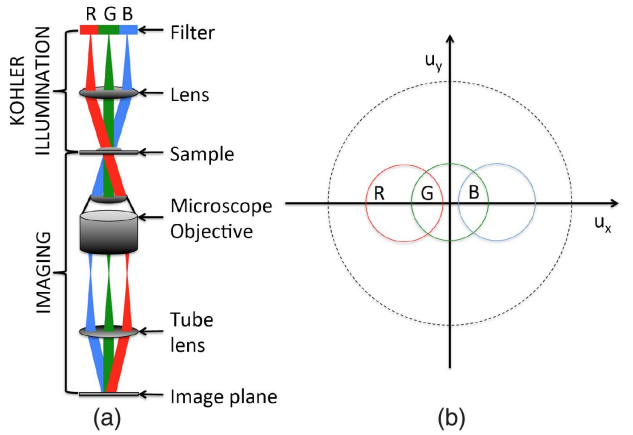

Fig. 1. (a) Illustration of optical Rheinberg illumination. Three color filters are placed at the back focal plane of the condenser lens. (b) Each of the three point sources illustrated in Fig. 1(a) independently contribute to image formation. In each of these three cases image formation results from bilinear contributions from within the supports shown in the spatial frequency domain. The radius of the circular supports shown in the figure is related to the pupil function of the microscope [36]. The dashed line represents the fundamental limit of resolution.

source illumination and the lens preceding the filter are not shown in the image.

Image formation in microscopy can be described using Fourier theory [35–38]. For the case of spatially coherent illumination, the image is given by the convolution of the input complex transmittance, $t(x)$, and the coherent point spread function of the optical system, $h(x)$, where x denotes the two-dimensional spatial coordinate system. This convolution can be described as a multiplication in the spatial frequency domain; i.e., the Fourier transform of the image is given by the Fourier transform of $t(x)$, which is denoted as $F(k)$, and the pupil function of the microscope, $P(k)$, where k denotes the 2D coordinates of the spatial frequency domain. In this case, the imaging system is linear in complex amplitude. For the case of incoherent illumination, the image formed by the microscope is given by the convolution of the intensity $|t(x)|^2$ and the incoherent point spread function of the optical system $|h(x)|^2$. Once again this can be described in terms of the Fourier transforms of these two functions; this time, however, image formation is linear in intensity.

For the case of a partially coherent imaging, such as that provided by Kohler illumination, image formation becomes more complex, and is no longer linear in either complex transmittance or intensity. For such a system, it can be assumed that the object is illuminated by an "incoherent" delta correlated light source propagating from the condenser pupil [29]. In the following derivation, it is assumed that the illumination is quasi-monochromatic; more specifically, it is assumed that for each of the different color filters in the illumination setup, the light that is transmitted is quasi-monochromatic around that filters line (band) pass wavelength. An extension of this analysis to polychromatic illumination is trivial. Unit magnification is assumed throughout the analysis. Initially, only a

single filter is considered; the illumination emerging from the filter plane has an intensity distribution $S(k)$. The image at the output of the microscope is given by

$$I(x) = \int S(k)\left|\int t(x')h(x-x')e^{j2\pi kx'}\mathrm{d}x'\right|^2\mathrm{d}k. \quad (1)$$

A simple interpretation of microscopic image formation using Kohler illumination now emerges; the image may be described as an incoherent superposition of the intensities produced by coherent plane wave illumination. In other words, each point (source), or delta functional in the filter plane can be viewed as a spatially coherent source that produces a coherent image as described above. The intensity of each of these coherent images is then superimposed to produce the final image. Equation (1) can also be rewritten in terms of their respective Fourier transforms:

$$I(x) = \iiint S(k)F(k_1)F^*(k_2) \times P(k+k_1)P^*(k+k_2)e^{j2\pi x(k_1-k_2)}\mathrm{d}k_1\mathrm{d}k_2\mathrm{d}k, \quad (2)$$

where $P(k) = |P(k)|e^{jkW(k)}$ is the coherent transfer function with the pupil function $P(k)$. For the majority of cases, $P(k)$ is given by a circ function with radius r, and the wavefront aberration $W(k)$. It is clear from Eq. (1) that the observed image intensity is not linear in the complex (specimen) transmittance. Furthermore, it can be seen from Eq. (2) that the intensity spectrum consists of the mixing of pairs of spatial frequencies in the amplitude spectrum of the specimen; each pair (k_1, k_2) produces a cosine term with a frequency given by $(k_1 - k_2)$, a complex amplitude given by $F(k_1)F^*(k_2)$, which determines the weight of this cosine in the final image as well as the phase shift of the cosine angle. For this reason, this type of image formation is said to be bilinear [29]. Separating the contribution of the specimen and the system to image formation leads to the concept of the transmission cross-coefficient [29,37,38],

$$\mathrm{TCC}(k_1,k_2) = \iint S(k)P(k+k_1)P^*(k+k_2)\mathrm{d}k, \quad (3)$$

which leads to a description of the transfer function for partially coherent image formation as follows:

$$I(x) = \iint F(k_1)F^*(k_2)\mathrm{TCC}(k_1,k_2)e^{j2\pi x(k_1-k_2)}\mathrm{d}k_1\mathrm{d}k_2. \quad (4)$$

The case is now considered where $S(k)$ is given by three different color filters, $S_R(k)$, $S_G(k)$, and $S_B(k)$, where R, G, and B denote red, green, and blue. If it is assumed that the sensor recording the image is independently sensitive to red, green, and blue light, Eqs. (3) and (4) can then be rewritten in terms of three independent transmission cross-coefficient terms as follows:

$$\mathrm{TCC}_i(k_1,k_2) = \iint S_i(k)P(k+k_1)P^*(k+k_2)\mathrm{d}k$$
$$I_i(x) = \iint F(k_1)F^*(k_2)\mathrm{TCC}_i(k_1,k_2)e^{j2\pi x(k_1-k_2)}\mathrm{d}k_1\mathrm{d}k_2, \quad (5)$$

where the index i in the above equations takes on three values R, G, and B. Here, it is assumed that the camera is capable of recording three independent images for red, green, and blue light by using a Bayer mask or a temporal filter. In terms of image formation, each of these three images can be considered independently by taking into account only the illumination emerging from the red, green, or blue filter.

The most common filter for Rheinberg illumination uses only two colors; a central circ function containing one color (e.g., red) while a surrounding ring contains a second color filter, (e.g., green). In this case, the image is made up of two independent color images, $I_R(x)$ and $I_G(x)$, as described in Eq. (5), where

$$\mathrm{TCC}_R(k_1,k_2) = \iint \mathrm{circ}_{r_1}(k)P(k+k_1)P^*(k+k_2)\mathrm{d}k$$
$$\mathrm{TCC}_G(k_1,k_2) = \iint [\mathrm{circ}_{r_2}(k) - \mathrm{circ}_{r_1}(k)]P(k+k_1)P^*(k+k_2)\mathrm{d}k, \quad (6)$$

in which r_1 and r_2 denote the radius of the inner and outer filters and circ(k) represents a circ function in the Fourier domain [36]. In this case, the red image will be formed by contributions of $F(k)$ from only lower spatial frequencies while the green image will be formed by contributions of $F(k)$ from only higher spatial frequencies. The resulting image shows a sharp contrast in color content for regions containing low-frequency background and higher-frequency cellular features.

In order to better understand the role of the filter distribution on image formation, a simple case is now considered where each of the three filters is represented by a single point source, as illustrated in Fig. 1(a), which are modeled by Dirac delta functional as follows:

$$S_G(k) = \delta(k),$$
$$S_R(k) = \delta(k-\alpha),$$
$$S_B(k) = \delta(k+\alpha), \quad (7)$$

where α denotes a shift in the k_x and k_y dimensions. The transmission cross-coefficient terms for the three different images are given by

$$\mathrm{TCC}_G(k_1,k_2) = P(k_1)P^*(k_2),$$
$$\mathrm{TCC}_R(k_1,k_2) = P(\alpha+k_1)P^*(\alpha+k_2),$$
$$\mathrm{TCC}_B(k_1,k_2) = P(-\alpha+k_1)P^*(-\alpha+k_2), \quad (8)$$

Although image formation is bilinear and is given by the sum of interference terms within the bounds of overlapping pupil functions, it is possible to make some interesting conclusions based on Eqs. (5) and (6). It is clear that image formation will result from contributions of the complex transfer function of the specimen $F(k)$ within the bounds of a pupil function $P(k)$ for the green image, $P(k+\alpha)$ for the red image, and $P(k-\alpha)$ for the blue image. In this discussion, the bilinear nature of image formation is not ignored; however, by dropping the variables k_1 and k_2 and considering only a single variable it is possible to focus only on the band of spatial frequencies within $F(k)$ that contribute to image formation (albeit in a non-linear manner based on interference terms).

In this way, it can considered that optical staining will be based on the spatial frequency distribution of the specimen, as illustrated in Fig. 1(b). In this simplified example, the red

image will be constructed from a finite band of spatial frequencies of $F(k)$ that are mostly negative in k_x, while the blue image is formed by contributions from a finite band of spatial frequencies of $F(k)$ that are mostly positive in k_x; finally, the green image is formed by contributions from a finite support of $F(k)$ around the origin. It must be noted that the maximum spatial frequencies that can contribute to image formation, denoted by the dashed line in Fig. 1(b), will be bounded by $\sqrt{k_x^2 + k_y^2} < 1/\lambda$, where λ is the wavelength of the quasi-monochromatic light. Any spatial frequency components outside of this area contribute only to rapidly attenuating evanescent waves [35,36].

In the following section, the theoretical analysis presented here is used as the basis for the development of a numerical algorithm that is capable of simulating the process of image formation in an optical microscope utilizing Rheinberg illumination.

3. DIGITAL SIMULATION OF RHEINBERG ILLUMINATION

Quantitative phase imaging techniques based on a partially coherent illumination, and digital holographic microscopy based on coherent illumination [17–19], both produce an image of the specimens complex transmittance, $t'(x)$, which it is assumed will be available as input to the algorithm under development in this section.

A. General Case

In the general case, the objective is to simulate optical Rheinberg illumination for a sample transmittance given by $t'(x)$; in terms of the original sample, *this is equivalent to first recording the quantitative phase image* $t'(x)$ using material holography [36] and then using this material hologram as the sample in an optical microscope utilizing Rheinberg illumination. The special case of simulating optical Rheinberg illumination of the actual original sample, with transmittance $t(x)$, is discussed in the next subsection. In order to simplify the analysis that follows, the discussion is based only on continuous variables; their discrete counterparts are briefly discussed later. For the general case, the red image can be generated as follows:

1. Select a number of parameters. These include (i) deciding on the number of pinholes in the filter, and for each one deciding their color and position. Thus, the user selects a set of N red pinhole positions: $[\alpha_{R1}, \alpha_{R2}, \ldots, \alpha_{RN}]$; (ii) deciding on the numerical aperture of the optical microscope that is being simulated. In simple terms this equates to selecting the radius, r_s, of the pupil function, $P_s(k)$, of the optical system to be simulated. Obviously $r_s \leq r$, since it will be impossible to improve on the resolution of the original image.
2. Simulate the illumination of $t'(x)$ with a plane wave of angle θ with respect to the optical axis, emerging from point source α_{R1}. The relationship between θ and α_{R1} is given by $\tan\theta = \alpha_{R1}/f$, where f is the focal length of the condenser lens. In the frequency domain, Step 2 is equivalent to shifting $F'(k)$ by an amount α_{R1}.
3. Simulate image formation in the microscope by convolving the image obtained in Step 2 with the point spread function of the microscope being simulated. In the frequency domain, Step 3 is equivalent to multiplying by $P_s(k)$.
4. Calculate the intensity of the resultant image.
5. Repeat Steps 2–4 for each of the $[\alpha_{R1}, \alpha_{R2}, \ldots, \alpha_{RN}]$ pinhole positions to obtain the final red image.

The blue and green images can be obtained in the same manner using different sets of pinhole positions. It must be noted that is possible for the shift in the frequency domain introduced in Step 2 to be large enough to result in $P_s(k)$ in Step 3 overlapping with no signal energy. Thus, it is important to judiciously select the pinhole positions, taking into account both the frequency support of the original image as defined by P as well as the support of P_s. A simple algorithm can now be defined that makes use of the discrete Fourier transform (DFT) [36,39], which can be efficiently calculated using the fast Fourier transform algorithm. The algorithm is illustrated in Fig. 2. The previously described steps can be rewritten in terms of a computational algorithm as follows. For the red image only:

1. Select the set of pixel coordinates $[\alpha_{R1}, \alpha_{R2}, \ldots, \alpha_{RN}]$ and pixel radius r_s, which is the radius of P_s.
2. Calculate the DFT of the input digital complex image t'.
3. Multiply the result of Step 2 with a binary mask given by a circular aperture of radius r_s and center coordinate α_{R1}. Then, calculate the inverse DFT.
4. Multiply each pixel value by its complex conjugate to obtain the intensity.
5. Repeat Steps 3–4 for each pinhole position given in Step 1 and add all of the resultant intensity images together to obtain the final red image.

In total, $N + 1$ DFTs must be calculated to generate the red image. The overall process is repeated for the blue and green

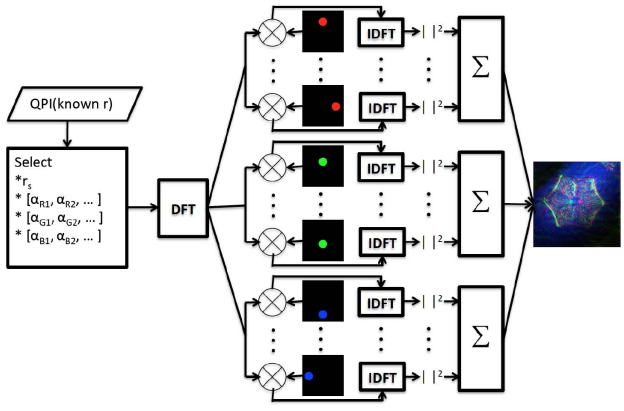

Fig. 2. Description of the algorithm that simulates optical Rheinberg illumination. Input to the algorithm is the quantitative phase image. The user selects the pinhole locations and the pupil radius for the optical microscope under simulation. A single DFT is calculated and stored for use as input to all of the remaining steps in the algorithm. For the red image, this DFT is multiplied by a sequence of different binary masks, each one associated with a different point source (pinhole) in the filter plane. In each case an inverse DFT is calculated and the resultant intensity is stored. All of these intensities are superimposed to generate the final red image. The same procedure is applied for the red and green cases, each with their own set of unique pinhole positions.

images, as illustrated in Fig. 2, and the final RGB image is obtained by combining these three independent images. It should be noted that the resolution of the final image will depend on the value of r_s.

B. Special Case: Simulation of Optical Rheinberg Illumination of the Original Transmittance $t(x)$

The general case described the situation where the original sample's transmittance $t(x)$ function is first recorded by a quantitative phase microscope with a complex point spread function $h(x)$, which provides a complex image $t'(x)$. The relationship between these three functions can be described in terms of their Fourier transforms as follows:

$$F'(k) = F(k)P(k). \tag{9}$$

Here, $P(k) = |P(k)|e^{jkW(k)}$ denotes the pupil function associated with the recording optical system, which is commonly assumed to be given by a circ function and the wavefront aberration $W(k)$ and $F(k)$ is the complex transfer function of the specimen. Going forward, this aberration is neglected (the effect of aberration can be reduced significantly using various compensation algorithms for quantitative phase imaging [20,21,40], and the pupil function is considered to be given only by a circ function with a radius $r \leq 1/\lambda$; i.e., it is assumed that the optical system introduces a spatially frequency cutoff less than or equal to the maximum permissible bandpass as described in Section 2. In this case, it is clear that complex transfer function of the original specimen, $F(k)$, is available up to some bound, and therefore, it is possible to simulate the process of optical Rheinberg illumination on that original specimen so long as the algorithm parameters are chosen judiciously. This will be true so long as $|\alpha| + r_s < r$ for all pinhole positions α, where r and r_s denote the radius of the pupil function associated with the recording microscope and the simulated microscope, respectively. It is clear that in order for the conditions of the special case to be met it is necessary that $r > r_s$ and therefore, the special case requires that the processed (color stained) image must be of lower resolution than the recorded image. In the next section results are shown for a number of diatom cells for both the general case and the special case.

4. RESULTS

A. Recording of Quantitative Phase Images

All of the quantitative phase images that were used to generate the results in this paper were recorded using an off-axis digital holographic microscope with the same architecture as that described in detail in [25]. This system uses a coherent laser with wavelength 633 nm. The CCD camera has pixel pitch equal to 4 μm in both spatial dimensions and a total pixel count given by 1024×1024. The complex transmittance is obtained by spatial filtering the real image in the DFT domain as outlined in [17]. The images were in general not recorded at the exact image plane; the images were refocused using numerical propagation, specifically, using the spectral method outlined in [22,23] and making use of autofocusing as described in [25] in order to determine the precise propagation distance. Aberration compensation was performed using the method described in [21], which involves capturing the complex transmittance of the illuminating beam (subject to the same processing as described for the sample) and dividing this into the complex transmittance recorded from the sample. This produces the final transmittance, which is input to the algorithm described in Section 3. Quantitative phase images are recorded of two diatom cells using two different microscope objectives (MOs): a 20× MO with NA = 0.45 and an oil immersion 63× with NA = 1.4. In the subsections that follow the results are presented for seven different Rheinberg illuminations applied to these quantitative phase images. The diatom cells are mounted in Naphrax diatom mountant (Brunel Microscopes, UK), which has a refractive index of 1.73.

B. General Case: Simulation of Rheinberg Illumination to Complex Transmittance Recorded from a Diatom Cell with 20 × /0.45 Magnification

Here, the results are presented for simulated Rheinberg illumination of the complex transmittance recorded from a diatom cell using a 20 × /0.45 MO. The raw hologram contains 1024×1024 pixels of size 4 μm and, therefore, the DFT of this image contains 1024×1024 pixels of size 0.244 mm^{-1}.

Taking into account the 20× magnification, the sampling interval of the image is given by 0.2 μm and the DFT has a sampling interval of 4.88 mm^{-1}. The complex valued real image comprises a circular section in the DFT plane with a radius of 120 samples. Therefore, $r = 120 \times 4.88$ mm^{-1} and the full spatial frequency bandwidth of intensity of the real image is given by $2r$, which is approximately 1171.2 line pairs per millimeter (lpm). This is approximately in agreement with the Rayleigh criterion [35,36], which predicts an optical resolution (the smallest distance between two observable points) to be equal to $0.61 \times \lambda/\text{NA} = 0.858$ μm. Spatial filtering involves isolating the area of approximately 240×240 samples within the DFT that contains the real image and preforming an inverse DFT. This complex image is then subject to numerical propagation and aberration compensation as described in the previous section; these two processes have no effect on the bandwidth of complex image, i.e., the DFT of the final complex transmittance image still comprises a circular support of radius r. The intensity and phase components of this complex transmittance image are shown in Figs. 3(a) and 3(b), respectively, following interpolation up to a size 2000×2000 by zero padding the DFT. A point of note is that this complex DFT must be zero padded up to a width that is at least double the bandwidth of the complex transmittance (i.e., at least 480 samples in this case) in order to guarantee that the intensity image shown in Fig. 3(a) is well sampled in the Nyquist sense [39].

Figure 3(d) shows the result of simulated Rheinberg illumination for the color filter illustrated in Fig. 3(c). As discussed in the previous section, this filter is simulated to exist in the back focal plane of the microscope condenser lens positioned for Kohler illumination. Each point source in the back focal plane of the condenser is transformed to a plane wave illumination in the sample plane. In order to reduce computational complexity the simulation involves only nine point sources in total, comprising eight red point sources at positions $[\alpha_{R1}, \alpha_{R2}, \ldots, \alpha_{R8}]$ located around a center green point source at position $\alpha_{G1} = (0, 0)$. Based on the discussion in Sections 2 and 3 we can expect this will result in the superposition of nine independent image intensities. Each of these nine images is obtained by

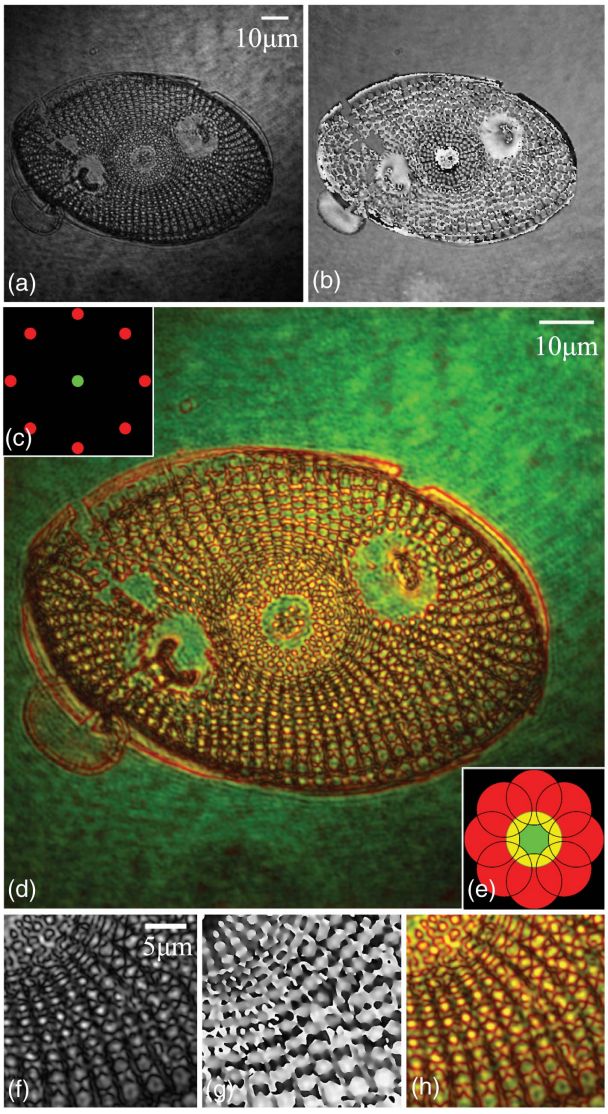

Fig. 3. Results for quantitative phase image of a diatom cell recorded with 20 × /0.45 MO. Shown here are the (a) intensity and (b) phase images of the recorded complex transmittance. (c) An illustration of the Rheinberg filter that is simulated to be in the back focal plane of a microscope condenser lens, which is made up of eight red point sources located around a center green point source. (d) The resulting image from simulated Rheinberg illumination. (e) Illustrates the filtering process that takes place in the DFT domain, for each of the independent point sources in the filter. This filtering process is illustrated in more detail in Fig. 4(a). Parts (f), (g), and (h) show the same image region for the image intensity, phase, and Rheinberg illumination cases, respectively.

spatial filtering different regions of the DFT of the complex transmittance function, as illustrated in Fig. 3(e), before returning to the spatial domain via an inverse DFT and taking the intensity of the resulting complex image. The overall algorithm describing this process is discussed in Section 3.A and illustrated in Fig. 2. More detail on the color filtering process that takes place is provided in Fig. 4. For comparison, Fig. 4 also contains three equivalent images of a small region of the cell relating to (f) the intensity, (g) the phase, and (h) the

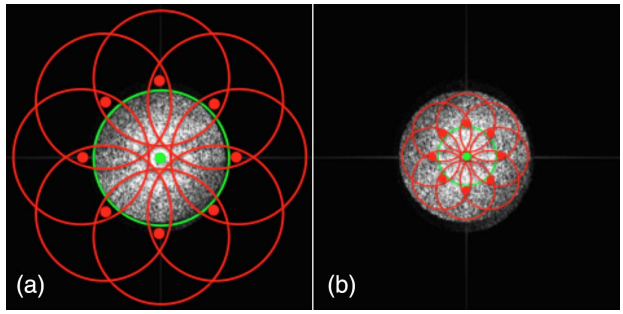

Fig. 4. Illustration of the color filtering that takes place in simulating Rheinberg illumination. (a) The general case: this image relates to the results shown in Fig. 3. The DFT of the complex transmittance that is input to the color staining algorithm is shown in the figure; the signal energy is contained in the center. The simulated color filter is shown as large red and green spots in the image, which represent point sources in the spatial frequency domain that are selected by the user. The user selects the radius of the circular filters, r_s, to be applied in the DFT domain. In this simulation, $r_s = r$. For each of the red masks, only a part of the spatial frequency support of the complex transmittance will contribute to the resulting intensity. The center positions of the red filters are chosen such that none of the red masks will overlap with the center of the DFT, which guarantees that regions with only low-frequency content, such as the background, will appear as green. (b) Illustrates the special case where each of the masks lies entirely within the spatial frequency support of the complex transmittance; the resulting image is shown later in Fig. 9 and discussed in Section 4.C.

Rheinberg image. It is clear that the color image provides superior contrast than the other two images. Figure 4(a) illustrates the spatial frequency filtering that takes place in the simulation that produces the color stained image shown above in Fig. 3(d). The DFT of the complex transmittance [with amplitude and phase shown in Figs. 3(a) and 3(b)] is shown in the figure; in total 650 × 650 samples are shown. The signal energy is contained in a circular area with radius $r = 120$ samples. The simulated color filter is shown as large red and green spots in the image, which represent point sources in the spatial frequency domain. The number, color, and position of these point sources are decided by the user. Also decided by the user, is the numerical aperture of the microscope being simulated, which in simple terms means that the user selects the radius of the circular filters, r_s, to be applied in the DFT domain. In this case it was chosen that $r_s = r$ and, therefore, each circular mask used in the algorithm has the same radius as $P(k)$. Since, for the single green filter, all of the signal energy is encompassed, it can be expected that the green image will be exactly equivalent to the gray-scale intensity image shown in Fig. 3(a), with no loss in resolution. For each of the red masks, only a part of the signal energy will contribute to the resulting intensity. It can be expected, therefore, that each of the red images will contain reduced resolution when compared to the green image. However, each of these eight red images will contain information that relates to different higher spatial frequency bands, none of which overlap with the low-frequency content at the center of the DFT; this is guaranteed if each red filter position obeys the following relationship: $|\alpha_{Ri}| > r$. In this case $|\alpha_{Ri}|$ is

selected to be 130 samples for each of the red filters. Thus, it can be expected that the color stained image will contain no red component in areas of the image that contain only low frequencies, such as background areas.

In this example the DFT was zero padded up to a size of 480 × 480 samples, which guarantees that the intensity image shown in Fig. 3(a) is well sampled in the Nyquist sense. In terms of the algorithm illustrated in Fig. 2, it is more efficient to maintain a small image size. Not shown in Fig. 2 is the interpolation of the color image as a final step, which can be applied arbitrarily by the user. Interpolation up to a larger size, such as the 2000 × 2000 image shown in Fig. 3(d), can be applied to each of the final red, green, and blue images that are output by the algorithm. Four more color stained images of the same QPI are shown in Fig. 5, where in each case different color filters are applied, shown in the top left of each figure. In all cases it was chosen that $r_s = r$ and $|\alpha|$ was chosen to be 130 samples for all of the various filters, except for the green filter placed at the origin. The resulting filtering that takes place in the DFT domain is illustrated in the bottom right of each figure. In all four cases the color filters contain three different colors—blue, green, and red—and in all cases a single green spot in the center is used to create the low spatial frequency background, similar to the previous case shown in Fig. 3. For the four cases, the surrounding multiple blue and red spots emphasize different image features related to different subcellular structure. In Fig. 5(a), the filter contains a single red point source and a single blue point source in the left and right of the horizontal spatial frequency axis, prospectively. Regions of the image that contain local frequency components that are captured in the corresponding circular filters will be stained with red and blue accordingly. Local spatial frequency can be related to the rate of change of the phase [36]; in this context, it can be inferred that image pixels with negative and positive phase gradients in the horizontal direction will be stained with blue and red color, respectively. There is clear evidence of predominantly red and green regions in the image, and these areas can be compared with the quantitative phase image in Fig. 3(b) in terms of phase gradient. Figure 6(a) provides an upsampled image of a cropped area of the image and there is clear evidence of color staining of subcellular features. In Fig. 5(b) the result is shown for which the filter contains a single red point source and a single blue point source in the upper and lower parts of the vertical spatial frequency axis, respectively. The resulting color stained image clearly shows red and blue color variation associated with subcellular features that are oriented in the vertical direction; features with phase gradient that are positive and negative are coded with red and blue color, respectively, and these features are clearly visible in Fig. 6(b). In Fig. 5(c) [and Fig. 6(c)] the color filter is made up of two red point sources placed in the horizontal dimension and two blue in the vertical. In this case image regions containing either positive or negative horizontal spatial frequencies will contain red staining, while blue staining will be applied to areas containing spatial frequency content in the vertical direction. Finally, in Figs. 5(d) and 6(d) the result is shown for a filter containing a circular distribution of red point sources, around which is another circular distribution of blue point sources. In this case, it can be expected that the blue stain will appear in image regions containing only higher frequencies in the image, while the red stain will appear in a lower band of spatial frequencies, but not so low as to extend to the origin.

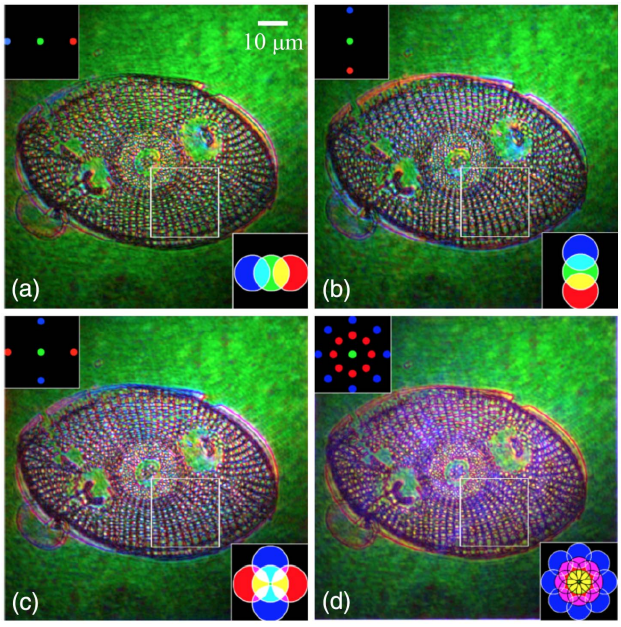

Fig. 5. Results of different simulated Rheinberg illuminations applied to the same QPI shown in the previous example. The color filter used in each simulation is shown the top left of each image, and the corresponding filters that are applied in the DFT domain are illustrated in the bottom right corner of each image. The individual parts, (a), (b), (c), and (d) are discussed in the text. The subsections from each of these images are shown in Fig. 6.

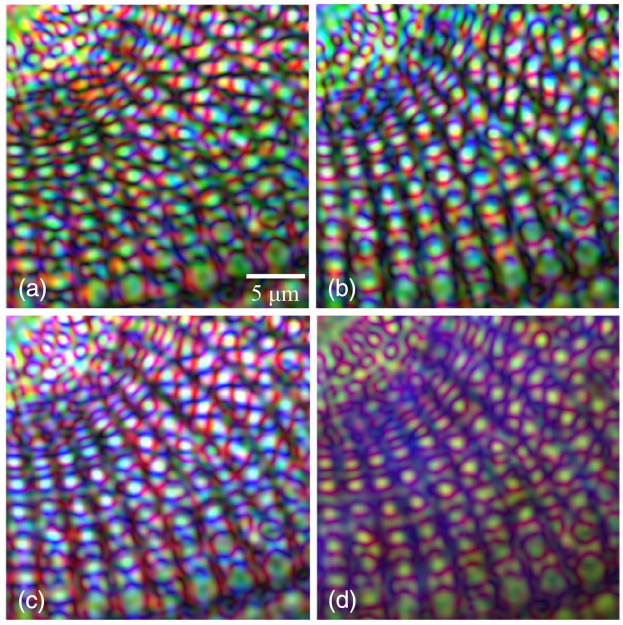

Fig. 6. Sections of images taken from Fig. 5 allowing for clearer inspection of the color staining of subcellular features, for each of the four color filters.

C. General Case: Simulation of Rheinberg Illumination to Complex Transmittance Recorded from a Diatom Cell with 63 × /1.4 Magnification

Here, the results are presented for simulated Rheinberg illumination of the complex transmittance recorded from a diatom cell using a 63 × /1.4 MO. As before, the raw hologram contains 1024 × 1024 pixels of size 4 μm and, therefore, the DFT of this image contains 1024 × 1024 pixels of size 0.244 mm^{-1}. Taking into account the 63× magnification, the sampling interval of the image is given by 63.49 nm and the DFT has a sampling interval of 15.372 mm^{-1}. The real image comprises a circular area in the DFT plane with a radius of 120 samples. Therefore, the full spatial frequency bandwidth of the real image is given by 2 × 120 × 15.372 mm^{-1}, which is approximately 3689.28 lpm. This is in agreement with the Rayleigh criterion, which predicts an optical resolution to be equal to 0.276 μm. Once again, the area of approximately 240 × 240 samples so cropped from the DFT, which contains the real image an inverse DFT, is performed. The resulting complex image is then subject to numerical propagation and aberration compensation. In all of the following simulations, the same values for r_s and α are selected as for the corresponding cases in the previous example. The intensity and phase components of this complex transmittance image are shown in Figs. 7(a) and 7(b), respectively, following interpolation up to a size 2000 × 2000 by zero padding the DFT. Figure 7(d) shows the result of simulated Rheinberg illumination for the color filter illustrated in Fig. 7(c). The corresponding filtering that takes place in the DFT domain is illustrated in Fig. 7(e). As for the previous case, Figs. 7(f)–7(h) compare the intensity image, the phase image, and the Rheinberg image for a region of the cell. Once again it is clear that the color image provides for higher-quality visualization of the cell structure. Four more color stained images of the same QPI are shown in Fig. 8, where in each case different color filters are applied, shown in the top left of each figure; the same color filters are used as in the previous example. The resulting filtering that takes place in the DFT domain is illustrated in the bottom right of each figure.

D. Special Case: Simulation of Optical Rheinberg Illumination of the Original Sample

All of the results presented so far have resulted from simulation using $r_s = r$, i.e., there is no loss in resolution for the (background) image. The other color images that are superimposed will all contain only part of the spatial frequency support, and will therefore have a reduced resolution; however, it must be noted that these color images will contain information from different spatial frequency bands. In Section 3.A this was introduced as the general case, which was equivalent to recording a material hologram of the complex transmittance and placing this in an optical microscope with a given Rheinberg filter and a specified NA. In Section 3.B it was proposed that it is possible to simulate optical Rheinberg simulation of the actual original sample under certain conditions. In light of the discussion thus far, these conditions can now be summarized as follows: all of the circular filters that are applied in the DFT domain must lie entirely within the spatial frequency support of the recorded complex transmittance, which is ensured with appropriate choice of r_s and the various pinhole positions.

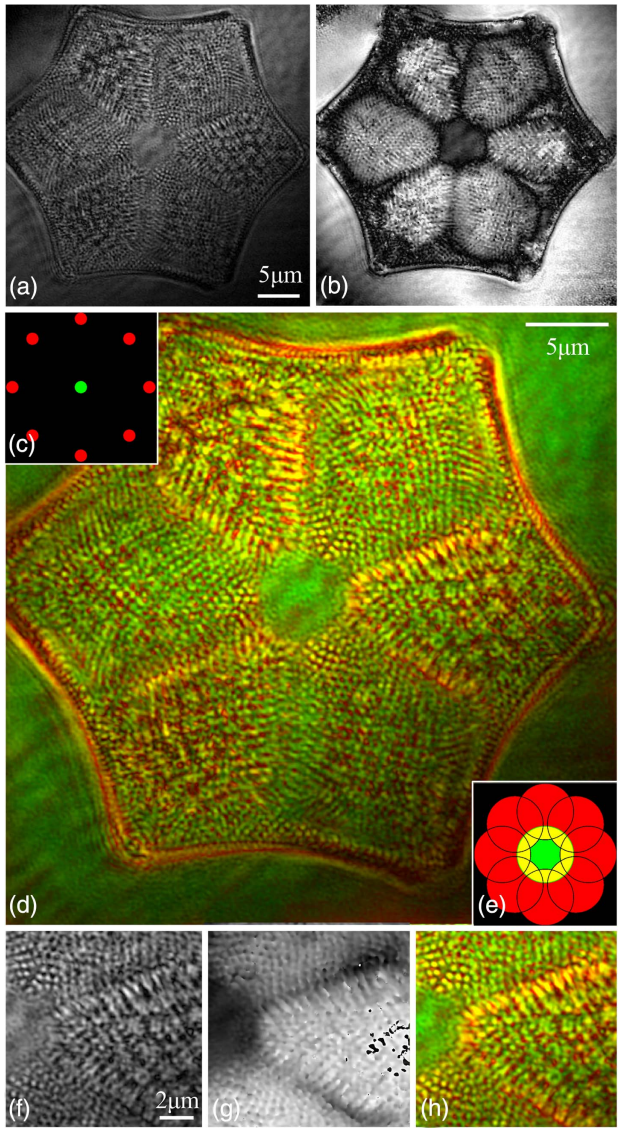

Fig. 7. Results for quantitative phase image of a diatom cell recorded with 63 × /1.4 MO. (a), (b) Intensity and phase images of the recorded complex transmittance. (c) Illustration of the Rheinberg filter used in the simulation. (d) Color stained image. (e) Illustration of the filtering process that takes place in the DFT domain, for each of the independent point sources in the filter. Parts (f), (g), and (h) show the same image region for the image intensity, phase, and Rheinberg illumination cases, respectively.

The result of color staining of the first QPI under the conditions of the special case is shown in Fig. 9(a). The color filter is shown in the top left corner of the image and the corresponding filtering masks applied to the DFT are illustrated in the bottom right corner. These masks are more accurately illustrated in Fig. 4(b). In this case r_s is chosen to be 60 samples and $|\alpha_{Ri}|$ is chosen to be 70 samples for all of the red pinholes. The resolution of the resulting image is, therefore, increased to 1.71 μm. This resolution is the same for each of the eight red images that are superimposed as well as the green background image, although each of these independent images will contain

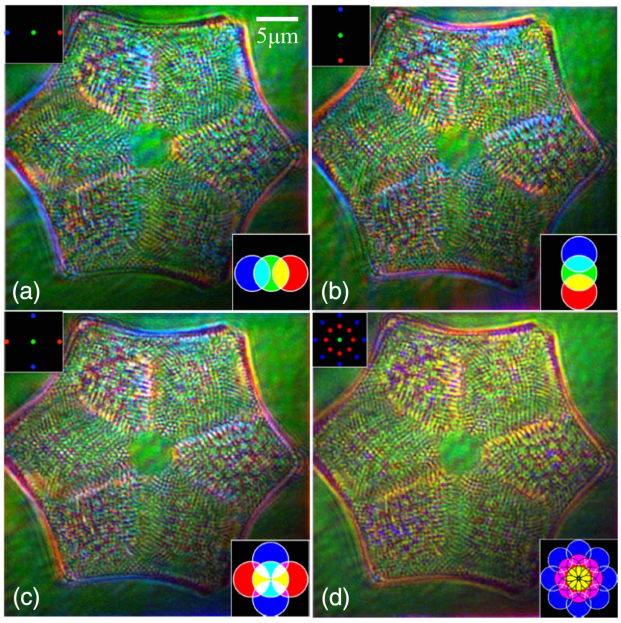

Fig. 8. Results of different simulated Rheinberg illuminations applied to the same QPI shown in the previous example. The color filter used in each simulation is shown in the top left of each image, and the corresponding filters that are applied in the DFT domain are illustrated in the bottom right corner of each image.

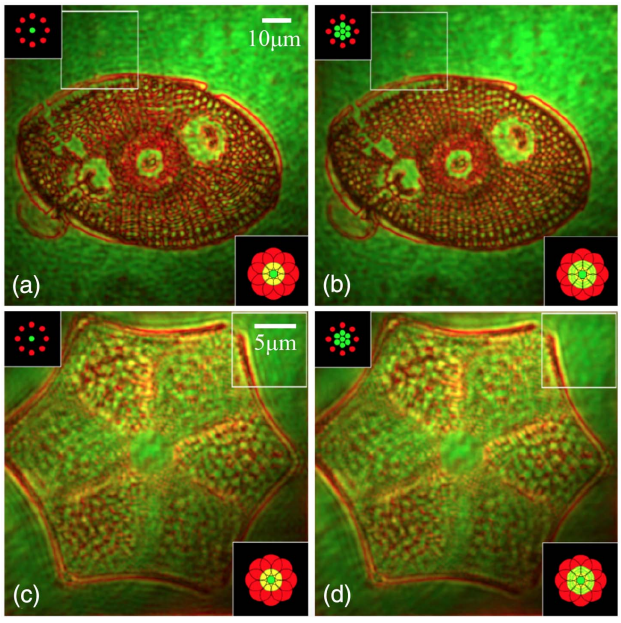

Fig. 9. (a) Result of color staining of the first QPI under the conditions of the special case. The color filter is shown in the top left corner and the corresponding filtering masks applied to the DFT are illustrated in the bottom right corner [note: these masks are more accurately illustrated in Fig. 4(b)]. (b) Shows a similar result except in this case a large number of green pinholes are used; due to the (partial) independence of the corresponding masks in the DFT domain, a reduction in spatial coherence is expected. (c), (d) Same set of results for the second QPI.

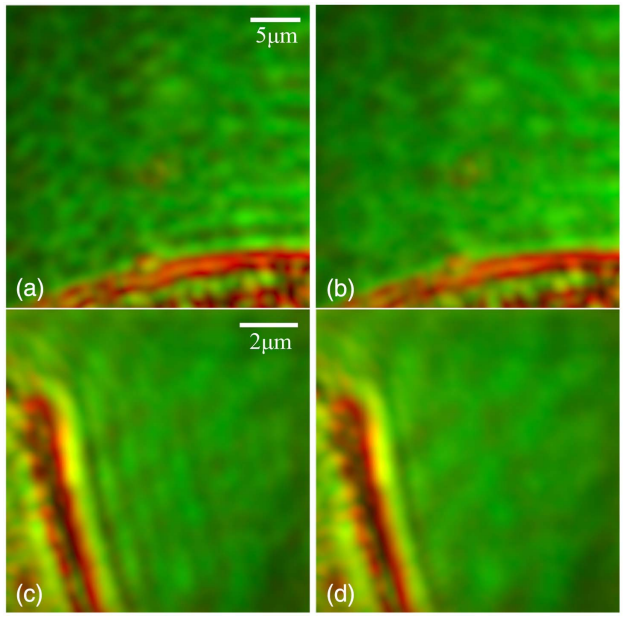

Fig. 10. Sections taken from corresponding images shown in the previous figure, highlighting a reduction in spatial coherence (but not resolution) due to the inclusion of additional independent filters.

information from different bands within the spatial frequency support of the image.

Figure 9(b) shows a similar result except that in this case an additional six green pinholes are added to the Rheinberg filter. The value of r_s is chosen to be the same as that for the previous example and the red pinholes have the same positions as before. The additional six green filters have positions $|\alpha_{Ri}|$ at a radius of 20 samples. Due to the partial independence of the seven green masks in the DFT domain, a reduction in spatial coherence is expected, although no improvement in resolution can be expected. A similar set of results for the second QPI is shown in Figs. 9(c) and 9(d); the resolution of these images is equal to 0.542 μm due to the different sampling interval for this case (see Section 4.C). In order to highlight the reduction in spatial coherence brought about by the inclusion of the six additional green filters, sections from Fig. 9 are magnified and shown in Fig. 10. In both bases there is clear evidence of a reduction in the noise due to spatial coherence. It should be noted that this has not resulted from a reduction in resolution; the comparable images have identical resolution for the green component. The reduction in coherence is due to the superposition of different (partially) independent filters applied in the spatial frequency domain, each containing (partially) different background images, which are then averaged together. This process could be repeated indefinitely in order to further reduce the noise resulting from spatial coherence in the background image; however, in order to increase the number of green images and to ensure the independence of each of these, the value of r_s would have to be reduced, which in turn would reduce the final image resolution.

5. DISCUSSION

In this paper a novel label-free color staining algorithm is proposed that can be applied to microscopic images of cells

recorded using quantitative phase microscopy. It must be noted that color coding in DHM/QPI is not new. Color coding of the quantitative phase image is commonly found in the literature. This approach usually involves simple thresholding, where color contrast is applied directly to the phase image based on the value of the phase. This approach should not be confused or conflated with the method proposed here, which is based on using a combination of different filters to generate different red, blue, and green image components.

For the two diatom cells investigated in this paper, it has been demonstrated that the color-coded Rheinberg image that is generated by the proposed algorithm provides superior image quality when compared with the image intensity as well as the quantitative phase image. The contrast of the image is improved as a result of the color information that is added to the various subcellular features as a function of their spatial frequency content. It is clear that the visualization of the cellular structure has been enhanced for both cases. More work is needed to investigate the potential of the technique for visualizing the structure of other types of cells, such as epithelial cells, which are commonly of interest in clinical cytology.

An interesting point of discussion on the difference between the optical and digital realizations of Rheinberg illumination relates to wavelength and resolution. In the optical case, different wavelengths are used to generate the different color components, whereas for the proposed algorithm only one wavelength is used to record the QPI images, and the different color images are generated using only this image as input. Since spatial resolution is directly proportional to wavelength, it can, therefore, be expected that the color components of an optical Rheinberg image may have different resolution to those of the simulated image, assuming the same color filter is used for both cases.

We conclude this paper with a comment on the applicability of the proposed algorithm in the life science community. A key requirement of the algorithm is the availability of the complex transmittance of the sample, which can be provided by digital holographic microscopy (as used in this paper) or some other form of quantitative phase imaging. In recent years, quantitative phase imaging has been shown to be possible with white light [15,16,26–31] and can be applied with existing commercial microscopes. These methods will likely replace existing phase contrast and DIC functionality in life science microscopes for the reason that the complex transmittance of the sample, available via QPI, permits other optical recording modalities (that do not involve staining or fluorescence) to be effectively simulated by numerically emulating the recording system. Another technique that falls under the category of QPI is lensless microscopy [32–34], which can recover the complex transmittance from a wide field area that is equal to that of the sensor [32–34]. It can be expected that the algorithm proposed here will be applicable to wide-field complex images recorded using this modality, and may, therefore, offer the potential to provide label-free color staining of thousands of biological cells within a large area (>20 mm^2) with image resolution on a par with that of high-NA modern microscope.

Funding. Science Foundation Ireland (SFI) (SFI/CDA/3667).

REFERENCES

1. M. Pluta and P. Maksymilian, *Advanced Light Microscopy* (Elsevier, 1988), Vol. **1**.
2. D. B. Murphy, *Fundamentals of Light Microscopy and Electronic Imaging* (Wiley, 2002).
3. F. Zernike, "Phase contrast, a new method for the microscopic observation of transparent objects," Physica **9**, 686–698 (1942).
4. C. Burch and J. Stock, "Phase-contrast microscopy," J. Sci. Instrum. **19**, 71–75 (1942).
5. F. Zernike, "How I discovered phase contrast," Science **121**, 345–349 (1955).
6. R. Allen and G. David, "The Zeiss-Nomarski differential interference equipment for transmitted-light microscopy," Z. Wiss. Mikrosk. Mikrosk. Tech. **69**, 193–221 (1969).
7. W. Lang, *Nomarski Differential Interference-Contrast Microscopy* (Carl Zeiss, 1982).
8. D. Murphy and M. Davidson, "Differential interference contrast (dic) microscopy and modulation contrast microscopy," in *Fundamentals of Light Microscopy and Digital Imaging* (Wiley-Liss, 2001), pp. 153–168.
9. J. W. Lichtman and J.-A. Conchello, "Fluorescence microscopy," Nat. Methods **2**, 910–919 (2005).
10. E. Harlow and D. Lane, *A Laboratory Manual* (Cold Spring Harbor Laboratory, 1988), Vol. **579**.
11. J. Rheinberg, "On an addition to the methods of microscopical research, by a new way optically producing color-contrast between an object and its background, or between definite parts of the object itself," JR Microsc. Soc. **16**, 373–388 (1896).
12. E. C. Samson and C. M. Blanca, "Dynamic contrast enhancement in widefield microscopy using projector-generated illumination patterns," New J. Phys. **9**, 363 (2007).
13. K. F. Webb, "Condenser-free contrast methods for transmitted-light microscopy," J. Microsc. **257**, 8–22 (2015).
14. C. Zuo, J. Sun, S. Feng, Y. Hu, and Q. Chen, "Programmable colored illumination microscopy (pcim): a practical and flexible optical staining approach for microscopic contrast enhancement," Opt. Lasers Eng. **78**, 35–47 (2016).
15. M. Mir, B. Bhaduri, R. Wang, R. Zhu, and G. Popescu, "Quantitative phase imaging," Prog. Opt. **57**, 133–217 (2012).
16. K. Lee, K. Kim, J. Jung, J. Heo, S. Cho, S. Lee, G. Chang, Y. Jo, H. Park, and Y. Park, "Quantitative phase imaging techniques for the study of cell pathophysiology: from principles to applications," Sensors **13**, 4170–4191 (2013).
17. E. Cuche, P. Marquet, and C. Depeursinge, "Simultaneous amplitude-contrast and quantitative phase-contrast microscopy by numerical reconstruction of Fresnel off-axis holograms," Appl. Opt. **38**, 6994–7001 (1999).
18. C. J. Mann, L. Yu, C.-M. Lo, and M. K. Kim, "High-resolution quantitative phase-contrast microscopy by digital holography," Opt. Express **13**, 8693–8698 (2005).
19. B. Kemper and G. von Bally, "Digital holographic microscopy for live cell applications and technical inspection," Appl. Opt. **47**, A52–A61 (2008).
20. T. Colomb, E. Cuche, F. Charrière, J. Kühn, N. Aspert, F. Montfort, P. Marquet, and C. Depeursinge, "Automatic procedure for aberration compensation in digital holographic microscopy and applications to specimen shape compensation," Appl. Opt. **45**, 851–863 (2006).
21. T. Colomb, J. Kühn, F. Charriere, C. Depeursinge, P. Marquet, and N. Aspert, "Total aberrations compensation in digital holographic microscopy with a reference conjugated hologram," Opt. Express **14**, 4300–4306 (2006).
22. K. M. Molony, B. M. Hennelly, D. P. Kelly, and T. J. Naughton, "Reconstruction algorithms applied to in-line Gabor digital holographic microscopy," Opt. Commun. **283**, 903–909 (2010).
23. D. Kelly, B. Hennelly, C. McElhinney, and T. Naughton, "A practical guide to digital holography and generalized sampling," Proc. SPIE **7072**, 707215 (2008).
24. P. Langehanenberg, B. Kemper, D. Dirksen, and G. Von Bally, "Autofocusing in digital holographic phase contrast microscopy on pure phase objects for live cell imaging," Appl. Opt. **47**, D176–D182 (2008).

25. X. Fan, J. J. Healy, and B. M. Hennelly, "Investigation of sparsity metrics for autofocusing in digital holographic microscopy," Opt. Eng. **56**, 053112 (2017).
26. Z. Wang, L. Millet, M. Mir, H. Ding, S. Unarunotai, J. Rogers, M. U. Gillette, and G. Popescu, "Spatial light interference microscopy (slim)," Opt. Express **19**, 1016–1026 (2011).
27. B. Bhaduri, H. Pham, M. Mir, and G. Popescu, "Diffraction phase microscopy with white light," Opt. Lett. **37**, 1094–1096 (2012).
28. A. Barty, K. Nugent, D. Paganin, and A. Roberts, "Quantitative optical phase microscopy," Opt. Lett. **23**, 817–819 (1998).
29. C. Zuo, J. Sun, J. Li, J. Zhang, A. Asundi, and Q. Chen, "High-resolution transport-of-intensity quantitative phase microscopy with annular illumination," Sci. Rep. **7**, 7654 (2017).
30. C. Zuo, Q. Chen, W. Qu, and A. Asundi, "High-speed transport-of-intensity phase microscopy with an electrically tunable lens," Opt. Express **21**, 24060–24075 (2013).
31. C. Zuo, Q. Chen, W. Qu, and A. Asundi, "Noninterferometric single-shot quantitative phase microscopy," Opt. Lett. **38**, 3538–3541 (2013).
32. W. Luo, Y. Zhang, Z. Göröcs, A. Feizi, and A. Ozcan, "Propagation phasor approach for holographic image reconstruction," Sci. Rep. **6**, 22738 (2016).
33. A. Ozcan and A. Greenbaum, "Maskless imaging of dense samples using multi-height lensfree microscope," U.S. patent 9,715,099 (25 July 2017).
34. Y. Rivenson, Y. Zhang, H. Günaydn, D. Teng, and A. Ozcan, "Phase recovery and holographic image reconstruction using deep learning in neural networks," Light: Sci. Appl. **7**, 17141 (2018).
35. M. Born and E. Wolf, *Principles of Optics: Electromagnetic Theory of Propagation, Interference and Diffraction of Light* (Elsevier, 2013).
36. J. W. Goodman, *Introduction to Fourier optics* (Roberts and Company, 2005).
37. H. H. Hopkins, "On the diffraction theory of optical images," Proc. R. Soc. London Ser. A **217**, 408–432 (1953).
38. C. Sheppard and A. Choudhury, "Image formation in the scanning microscope," Opt. Acta: Int. J. Opt. **24**, 1051–1073 (1977).
39. R. Bracewell, *The Fourier Transform and Its Applications* (McGraw-Hill, 1965), Vol. **5**.
40. T. Colomb, F. Montfort, J. Kühn, N. Aspert, E. Cuche, A. Marian, F. Charrière, S. Bourquin, P. Marquet, and C. Depeursinge, "Numerical parametric lens for shifting, magnification, and complete aberration compensation in digital holographic microscopy," J. Opt. Soc. Am. A **23**, 3177–3190 (2006).